Author Manuscript

Author Manuscript

Author Manuscript

Author Manuscript

HHS Public Access

Author manuscript

Nat Biomed Eng. Author manuscript; available in PMC 2018 October 09.

Published in final edited form as:

Nat Biomed Eng. 2018 April ; 2(4): 215–226. doi:10.1038/s41551-018-0217-y.

Magnetic resonance multitasking for motion-resolved quantitative cardiovascular imaging

Anthony G. Christodoulou[1,2], **Jaime L. Shaw**[1,3], **Christopher Nguyen**[1,†], **Qi Yang**[1,4], **Yibin Xie**[1], **Nan Wang**[1,3], and **Debiao Li**[1,3,*]

[1]Biomedical Imaging Research Institute, Cedars-Sinai Medical Center, Los Angeles, California, USA

[2]Smidt Heart Institute, Cedars-Sinai Medical Center, Los Angeles, California, USA

[3]Department of Bioengineering, University of California Los Angeles, Los Angeles, California, USA

[4]Department of Radiology, Xuanwu Hospital, Beijing, China

Abstract

Quantitative cardiovascular magnetic resonance (CMR) imaging can be used to characterize fibrosis, oedema, ischaemia, inflammation and other disease conditions. However, the need to reduce artefacts arising from body motion through a combination of electrocardiography (ECG) control, respiration control, and contrast-weighting selection makes CMR exams lengthy. Here, we show that physiological motions and other dynamic processes can be conceptualized as multiple time dimensions that can be resolved via low-rank tensor imaging, allowing for motion-resolved quantitative imaging with up to four time dimensions. This continuous-acquisition approach, which we name cardiovascular MR multitasking, captures — rather than avoids — motion, relaxation and other dynamics to efficiently perform quantitative CMR without the use of ECG triggering or breath holds. We demonstrate that CMR multitasking allows for T_1 mapping, T_1-T_2 mapping and time-resolved T_1 mapping of myocardial perfusion without ECG information and/or in free-breathing conditions. CMR multitasking may provide a foundation for the development of setup-free CMR imaging for the quantitative evaluation of cardiovascular health.

Users may view, print, copy, and download text and data-mine the content in such documents, for the purposes of academic research, subject always to the full Conditions of use: http://www.nature.com/authors/editorial_policies/license.html#terms

*Correspondence should be addressed to D.L. (Debiao.Li@cshs.org).

†Now also with the Cardiovascular Research Center, Massachusetts General Hospital, Harvard Medical School, Charlestown, Massachusetts, USA

AUTHOR CONTRIBUTIONS

A.G.C. conceived of the imaging framework, wrote the reconstruction and parameter fitting software, programmed the pulse sequence sampling scheme, performed the analysis, and prepared the majority of the manuscript. A.G.C., J.L.S., and D.L. designed the native T_1 mapping and first-pass myocardial perfusion T_1 mapping method and experiments, which J.L.S. and A.G.C. conducted. C.N. designed the T2IR preparation pulse and programmed it into the pulse sequence. A.G.C., Y.X., N.W., C.N., J.L.S., and D.L. designed the T_1-T_2 mapping method and healthy volunteer experiments, which A.G.C., J.L.S., and C.N. conducted; A.G.C., Q.Y., and D.L. designed the patient T_1-T_2 mapping experiments, which Q.Y. conducted. J.L.S performed the myocardial T_1 reconstructions. A.G.C. performed the T_1-T_2 and first-pass myocardial perfusion T_1 mapping reconstructions. All authors reviewed and edited the manuscript. D.L. supervised the entire work.

COMPETING INTERESTS

D.L., A.G.C., J.L.S., Y.X. and C.N. have a provisional patent application entitled “Low-rank tensor imaging for multidimensional cardiovascular MRI” (USSN 15/495,588).

Author Manuscript Author Manuscript Author Manuscript Author Manuscript

Quantitative cardiovascular MR (CMR) imaging has the potential to perform a wide range of diagnostic measurements in the heart, providing reproducible, accurate assessments of heart function and anatomy for diagnosing and monitoring cardiovascular diseases in humans and in animal models. For example, quantification of the nuclear magnetic resonance (NMR) relaxation constants T_1 and T_2 is promising for cardiovascular tissue characterization, revealing fibrosis, oedema, inflammation, and more[1, 2]; quantification of myocardial blood flow (MBF) through myocardial perfusion imaging is promising for diagnosing ischemia and coronary artery disease[3]. However, imaging in the presence of various overlapping dynamic processes — both physiological (e.g., cardiac and respiratory motion) and physical (e.g., T_1 and T_2 relaxation) — is a major technical challenge which has complicated the imaging procedure and prevented widespread adoption of quantitative CMR.

The conventional strategy to handle the overlapping dynamics involved in cardiovascular imaging has been to apply a complicated mixture of electrocardiography (ECG) control, breath holding, and/or short acquisition bursts to “freeze” as many dynamics as possible. This typically means choosing one dynamic at a time, forgoing useful information about the remaining dynamics and requiring pauses in between acquisition bursts. As a result, the standard cardiac exam consists of a prolonged, inefficient sequence of scans, each of which applies a different combination of freezing mechanisms targeting different dynamics. Furthermore, these freezing mechanisms can be unreliable (e.g., ECG triggering) or uncomfortable (e.g., breath holds), and the use of multiple breath holds results in misalignment between scans, complicating image fusion for comprehensive analysis. More importantly, this overall strategy does not work properly for particularly unhealthy subjects who have cardiac arrhythmias or difficulty holding their breath. Respiratory gating has been used to eliminate the effect of respiratory motion during free-breathing data acquisition, but the imaging efficiency is low, resulting in prolonged imaging time.

This work introduces *MR multitasking*, a continuous-acquisition framework which can simultaneously resolve the many overlapping dynamics involved in quantitative cardiovascular imaging. MR multitasking conceptualizes different sources of image dynamics as different time dimensions, resolving multiple time dimensions (or “tasks”) using a low-rank tensor (LRT) imaging method specifically designed to address the unique challenges of cardiovascular imaging. This efficient, reliable, and flexible imaging framework solves several long-standing problems in CMR. By using multitasking to capture (rather than avoid) motion, relaxation, and other dynamics, it becomes possible to perform quantitative CMR without the use of ECG triggering, breath holds, etc. Its ability to perform time-resolved T_1 mapping corrects the signal saturation problem in dynamic contrast enhanced (DCE) imaging, which is a major confounder of single-bolus flow quantification[4]. It simplifies workflow by integrating multiple capabilities into a single scan, allowing simultaneous acquisition of multiple co-registered parametric maps for comprehensive characterization of the cardiovascular tissue throughout the entire cardiac and respiratory cycles. Most importantly, it provides a potential avenue for imaging patients and subjects who would have difficulty receiving a conventional CMR exam due to breath hold difficulties and/or arrhythmias.

Author Manuscript Author Manuscript Author Manuscript Author Manuscript

A major technical challenge of multidimensional MRI is that scan times grow exponentially with the number of dimensions, a phenomenon known as the "curse of dimensionality". The LRT image model allows MR multitasking to bypass this phenomenon, exploiting the correlation between images at different time points to reduce sampling requirements. LRT imaging is not the only approach to reduced sampling (notable complementary approaches include compressed sensing[5] and MR fingerprinting[6]), but low-rank tensors are especially well-suited to multidimensional imaging: low-rank tensor degrees of freedom (and therefore their required scan times) scale approximately linearly with the number of dimensions rather than exponentially[7]. The multidimensional nature of LRT imaging distinguishes multitasking from other fast quantitative imaging methods such as MR fingerprinting, which does not resolve motion or DCE, requiring ECG triggering and breath holds when applied to cardiac imaging[8]. Conversely, although compressed sensing has proved useful for motion-resolved multidimensional imaging with cardiac and respiratory time dimensions (e.g., XD-GRASP[9]), these two time dimensions alone are not enough to perform quantitative imaging. This paper demonstrates motion-resolved quantitative imaging with as many as four time dimensions, a feat made possible by the exceptional scalability of low-rank tensors.

Low-rankness in various MRI applications has been well-established through work on low-rank matrix imaging involving only one time dimension[10–16], but there has so far been only limited exploration of low-rank tensors for high-dimensional MRI[17–22]. Cardiovascular imaging provides unique challenges preventing direct application of previous LRT imaging approaches, namely that physiological time dimensions cannot be precisely sampled without ECG and respiratory control — precluding approaches requiring specific sampling patterns[19–22] — and that large tensor sizes prevent unfactored tensor recovery[17, 18] on most machines. We have therefore developed a new LRT imaging strategy specifically for CMR multitasking, comprising: 1) a low-rank tensor image model exploiting image correlation along the direction of each physiological and physical time dimension; 2) a non-ECG data acquisition strategy featuring minimal gaps in acquisition and frequent collection of auxiliary subspace training data; and 3) a factored tensor reconstruction approach which enforces the LRT model in two efficient steps. The results of this method demonstrate and evaluate several of the new capabilities enabled by CMR multitasking: non-ECG, free-breathing T_1 mapping in the myocardium; non-ECG, free-breathing joint T_1-T_2 mapping in the myocardium; and non-ECG, time-resolved T_1 mapping during DCE, including first-pass myocardial perfusion T_1 mapping.

RESULTS

Imaging framework

CMR multitasking represents a set of cardiovascular images as a multidimensional tensor (or array) with one dimension indexing voxel location (i.e., combining the spatial dimensions) and the others indexing N different time dimensions (Fig. 1a), each corresponding to a different "task" to be imaged (e.g., T_1 recovery, T_2 decay, cardiac motion, respiratory motion, and/or DCE). By modelling this tensor as low-rank[10], we describe and exploit image correlation laterally along each time dimension and diagonally throughout the multidimensional temporal space, reducing the images to the product of a small core tensor

Author Manuscript Author Manuscript Author Manuscript Author Manuscript

and $N+1$ factor matrices containing basis functions[7] (Fig. 1b, Supplementary Fig. 1). These model components have far fewer elements than the total number of elements in the images, reducing data acquisition requirements and allowing highly accelerated scans. Data were acquired by interleaving sparsely sampled image data with auxiliary subspace training data that frequently samples a subset of **k**-space. A memory- and time-efficient factored approach was developed for image reconstruction, wherein the core tensor and N temporal factor matrices were estimated from the subspace training data, and the spatial factor matrix was recovered by fitting the core tensor and temporal factor matrices to the remainder of the measured data.

Native myocardial T_1 mapping

Quantification of the spin–lattice relaxation time constant T_1 can characterize myocardial tissue, detecting and measuring fibrosis, protein deposition, fat infiltration, and extracellular volume fraction (when used in conjunction with a gadolinium-based contrast agent), among other biologically and clinically relevant processes and measurements[1, 23]. T_1 mapping is performed by collecting multiple images with different T_1 contrast weightings from which a spatial map of T_1 values are then calculated. Current myocardial T_1 mapping techniques[24–27] rely on ECG synchronization and breath holding as a means of isolating the effects of T_1 relaxation. CMR multitasking eliminates the need for ECG and respiratory control, measuring a heart-rate–independent set of contrasts, and enables T_1 cine maps (i.e., cardiac-resolved T_1 maps).

Here we demonstrate T_1 mapping using CMR multitasking, assessing the repeatability and accuracy in a mid-ventricular short-axis slice against modified Look–Locker inversion recovery (MOLLI) 5(3)3[28], a leading ECG-triggered, breath-held method. A total of $n = 10$ healthy volunteers were imaged, each undergoing three scans each of MOLLI and CMR multitasking, both at 1.7 mm in-plane spatial resolution. MOLLI imaged eight heart-rate-dependent inversion times at the end-diastole cardiac phase and end-expiration respiratory phase; the resulting eight images were used to produce a T_1 map (Fig. 2c–d). The CMR multitasking method applied an inversion recovery (IR)–prepared fast low-angle shot (FLASH) sequence and imaged three time dimensions, measuring 344 heart-rate–independent inversion times up to 2.5 s (avoiding direct view sharing of data from different inversion times) for 16 cardiac phases and five respiratory phases (Fig. 2a–b, Supplementary Movie 1). This resulted in a total of 344*16*5=27,520 images from one minute of data acquisition. Compared to Cartesian Nyquist sampling of 27,520 images, this corresponds to an acceleration factor of R=267; if the inversion times were instead binned to only eight inversion times, this would correspond to R=6.2. T_1 maps were then calculated for the end-diastolic cardiac phase and end-expiration respiratory phase to match the MOLLI motion states.

Healthy diastolic T_1 values in the six American Heart Association (AHA)–defined mid-ventricular myocardial segments per subject for MOLLI (1237 ± 53 ms) and IR-FLASH CMR multitasking (1225 ± 75 ms) were within the published normal range at 3 T[29]. Comparison of the two methods (Fig. 2g–h) showed a positive correlation (r=0.59, Pearson's correlation coefficient) with no statistically significant bias (p=0.13, two-sided t-test). The

Author Manuscript Author Manuscript Author Manuscript Author Manuscript

variation of mean T_1 over the six segments (Fig. 2e–f) was highly correlated between methods (r=0.97, Pearson's correlation coefficient). Both methods demonstrated low root-mean-square (RMS) within-segment standard deviation (WSSD) and coefficient of variation (CoV), indicating good repeatability (MOLLI: 31 ms WSSD, 2.5% CoV; CMR multitasking: 59 ms WSSD, 4.8% CoV).

Because MOLLI is known to be reproducible but not necessarily accurate for T_1 mapping[30, 31], IR-FLASH multitasking was also compared to ground truth measurements in ten phantom vials placed along the chest of a healthy volunteer. Cardiac- and respiratory-resolved IR-FLASH multitasking was performed for a three-chamber cardiac view perpendicular to the vials (Fig. 3a); the vials moved with the chest wall during respiration. The multitasking T_1 values in the vials were compared to ground truth T_1 values (Fig. 3b–c) calculated from a series of IR spin echo (IRSE) images prior to their placement on the subject's chest. Multitasking and IRSE T_1 measurements demonstrated high positive correlation (r=0.993, Pearson's correlation coefficient) with no statistically significant bias (p=0.11, two-sided t-test).

Native myocardial T_1-T_2 mapping

Quantification of the spin–spin relaxation time constant T_2 detects and characterizes myocardial oedema, ischemia, and inflammation, and more[2]. T_2 mapping provides complementary information to T_1 mapping, making joint T_1-T_2 mapping very promising for comprehensive myocardial tissue characterization. Currently, T_1-T_2 mapping can be performed via ECG-triggered, breath hold techniques, either mapping T_2 separately[2] from T_1 (resulting in unaligned maps), or jointly[8, 32–35]. Joint T_1-T_2 mapping CMR multitasking requires no ECG and respiratory control, providing aligned T_1 and T_2 maps at multiple cardiac phases.

This section demonstrates T_1-T_2 mapping using CMR multitasking (Fig. 4a–c), measuring repeatability and accuracy in a mid-ventricular short-axis slice against T_1 values from MOLLI 5(3)3 (Fig. 4d) and T_2 values from a T_2-prepared steady-state free precession (T_2prep-SSFP) mapping method[2] (Fig. 4e). Three scans each of MOLLI, T_2prep-SSFP, and the proposed CMR multitasking method were performed in n = 10 healthy volunteers. All three methods were performed at 1.7 mm in-plane spatial resolution. MOLLI imaged eight inversion times and T_2prep-SSFP imaged three T_2prep durations, both using ECG triggering to image at the end-diastole cardiac phase and using breath holds to image at the end-expiration respiratory phase. The non-ECG, free-breathing CMR multitasking method applied a hybrid T_2prep/IR (T2IR)–prepared FLASH sequence to generate multiple T_1-T_2 contrasts. Four time dimensions were imaged, measuring 344 inversion times (up to 2.5 s) for each of five T_2 prep durations (12 ms, 20 ms, 30 ms, 40 ms, and 50 ms) at 16 cardiac phases and five respiratory phases, for a total of 344*5*16*5=137,600 images from 88 s of data acquisition. Compared to Cartesian Nyquist sampling of 137,600 images, this corresponds to R=914; if the inversion times were instead binned to only eight inversion times, this would correspond to R=21. T_1 and T_2 were jointly fit at the end-diastolic cardiac phase and end-expiration respiratory phase to match the motion states of the reference methods.

Author Manuscript Author Manuscript Author Manuscript Author Manuscript

Healthy diastolic T_1 values in six myocardial segments per subject for MOLLI (1244 ± 48 ms) and T2IR-FLASH CMR multitasking (1216 ± 67 ms) were within the published normal range at 3 T[29]. Comparison of multitasking to MOLLI (Fig. 4h–i) indicated a positive correlation (r=0.72, Pearson's correlation coefficient) and a –28 ms bias (p<0.001, two-sided t-test). The variation of mean T_1 over the six segments (Fig. 4f–g) was correlated between methods (r=0.82, Pearson's correlation coefficient). Both methods demonstrated low RMS-WSSD and CoV, indicating good repeatability (MOLLI: 25 ms WSSD, 2.0% CoV; CMR multitasking: 77 ms WSSD, 6.3% CoV).

As in the case of IR-FLASH T_1 mapping, T_1 values from T2IR-FLASH multitasking were also compared to IRSE ground truth values for vials placed along a subject's chest to address the established accuracy issues with MOLLI. The mean T_1 values in the vials were compared to the IRSE T_1 values (Fig. 3d–e), demonstrating high positive correlation (r=0.997, Pearson's correlation coefficient) with a −51 ms bias (p=0.02, two-sided t-test).

Healthy diastolic T_2 values in six myocardial segments per subject for T_2prep-SSFP mapping (50.0 ± 3.1 ms) and CMR multitasking (47.8 ± 4.9 ms) were also within the published normal range at 3 T[29]. Comparison of multitasking to T_2prep-SSFP mapping (Fig. 4l–m) showed a positive correlation (r=0.47, Pearson's correlation coefficient) with a −2.2 ms bias (p<0.001, two-sided t-test). The variation of mean T_2 over the six segments (Fig. 4j–k) was nonsignificant for both methods (MOLLI: p=0.60, CMR multitasking: p=0.58, one-way ANOVA) but positively correlated between methods (r=0.49, Pearson's correlation coefficient). Both methods demonstrated low RMS-WSSD and CoV, indicating good repeatability (T_2prep-SSFP: 3.2 ms WSSD, 6.4% CoV; CMR multitasking: 5.4 ms WSSD, 11.4% CoV).

T_1-T_2 mapping was also evaluated in a pilot study of n = 10 patients with acute myocardial infarction (MI). One scan each of MOLLI 5(3)3, T_2prep-SSFP mapping, and T2IR-FLASH multitasking were collected for native parameter mapping. Late gadolinium enhancement (LGE) imaging was subsequently performed to assess the extent of MI. The T_1 values in six myocardial segments per subject from CMR multitasking (1213 ± 145 ms) were compared to MOLLI (1250 ± 142 ms), showing a positive correlation (r=0.80, Pearson's correlation coefficient) and a −37 ms bias (p=0.003, two-sided t-test) (Fig. 5a–d). The T_2 values from CMR multitasking (45.5 ± 9.3 ms) were compared to T_2prep-SSFP mapping (42.9 ± 6.8 ms), showing a positive correlation (r=0.67, Pearson's correlation coefficient) and a +2.5 ms bias (p=0.007, two-sided t-test). Native T_1 mapping produced higher T_1 values in LGE-positive segments (MOLLI LGE+: 1383 ± 187 ms, LGE−: 1219 ± 110 ms, p<0.001, two-sided t-test; Multitasking T_1 LGE+: 1319 ± 208 ms, LGE−: 1188 ± 116 ms, p=0.006, two-sided t-test). Both T_1 mapping methods were predictive of LGE status: the area under the curve (AUC) of the receiver operating characteristic (ROC) curve equalled 0.74 for MOLLI and 0.70 for multitasking (Fig. 5g). T_2 mapping produced higher T_2 values in LGE-positive segments (T_2prep-SSFP LGE+: 50.6 ± 8.9 ms, LGE−: 41.2 ± 4.8 ms, p<0.001, two-sided t-test; Multitasking T_2 LGE+: 56.2 ± 10.3 ms, LGE−: 43.0 ± 7.1 ms, p<0.001, two-sided t-test). Both T_2 mapping methods were predictive of LGE status: the ROC AUC equalled 0.77 for T_2prep-SSFP mapping and 0.80 for multitasking (Fig. 5h). The potential value of measuring both T_1 and T_2 using CMR multitasking is illustrated by a 2D feature space of

Author Manuscript Author Manuscript Author Manuscript Author Manuscript

multitasking T_1 and T_2 values (Fig. 5i), for which the pictured decision boundary yielded 91% sensitivity and 91% specificity — higher maximum accuracy for the pilot data than either measurement provided alone, regardless of method.

The results also offer a preliminary demonstration of some of the additional potential benefits of cardiac- and respiratory-resolved quantitative CMR beyond freedom from ECG triggering and breath-holding. These include the potential to assess ventricular function without requiring a separate cine imaging scan (Fig. 6a–b), to measure changes in apparent NMR relaxation time constants throughout the cardiac cycle (Fig. 6c), and to measure changes in cardiac geometry throughout the respiratory cycle (Fig. 6d). The potential to assess cardiac function was evaluated by comparing in-slice left ventricular (LV) areas from dark-blood T2IR-FLASH multitasking images to LV areas from retrospectively ECG-gated bSSFP cine images in the healthy cohort. End-diastolic LV area (EDLVA) measurements from multitasking (20.1 ± 2.6 cm^2) and ECG-gated cine imaging (21.3 ± 2.2 cm^2) were highly correlated (r=0.92, Pearson's correlation coefficient), with multitasking demonstrating a −1.2 cm^2 bias (p=0.04, two-sided t-test). End-systolic LV area (ESLVA) measurements from multitasking (10.0 ± 2.4 cm^2) and ECG-gated cine imaging (9.9 ± 2.2 cm^2) were highly correlated (r=0.91, Pearson's correlation coefficient), with no statistically significant bias (p=0.85, two-sided t-test).

First-pass myocardial perfusion T_1 mapping

First-pass myocardial perfusion imaging is a powerful tool for assessing blood flow in the myocardium, diagnosis of ischemia and coronary artery disease. The relaxation rate $R_1=1/T_1$ increases by an amount proportional to local concentration of gadolinium (Gd)-based contrast agent, so time-resolved, T_1-weighted imaging can be employed to image DCE during the first pass of a bolus of Gd. Most first-pass perfusion imaging scans employ ECG triggering to collect one magnetization-prepared image per cardiac cycle[3], but recent methods have achieved imaging without ECG triggering, using steady-state pulse sequences rather than magnetization preparation to generate T_1 contrast[36, 37].

Unfortunately, neither of these approaches allows quantification from a single scan. This is because T_1-weighted signal intensity has a nonlinear response to R_1 — saturating at high Gd concentrations such as those in the blood pool at peak enhancement — violating the conventional assumptions of linearity that are used to quantify MBF[38]. Quantitative myocardial perfusion MRI is therefore commonly performed using two scans with two boluses of contrast[4]: the first bolus contains a small dose of contrast agent, inducing an approximately linear signal response in the blood pool at the expense of poor signal response in the myocardium, and the second bolus contains a large dose of contrast agent, inducing an approximately linear signal response in the myocardium (which is less susceptible to signal saturation) at the expense of nonlinearity in the blood pool. Quantification is then performed by assuming that there are no changes in physiology between boluses.

CMR multitasking addresses both ECG dependence and signal nonlinearity by adding a cardiac motion time dimension and a saturation recovery time dimension, respectively, to the conventional DCE time dimension. Resolving cardiac motion provides freedom from ECG

Author Manuscript Author Manuscript Author Manuscript Author Manuscript

triggering and allows analysis at multiple cardiac phases. Imaging multiple saturation times allows quantification from a single bolus of contrast[39], as the resulting time-resolved T_1 maps can be converted to time-resolved contrast agent concentration maps, which directly accounts for signal nonlinearity.

We demonstrate this first-pass myocardial perfusion T_1 mapping here, assessing intrasession reproducibility in a mid-ventricular short-axis slice at 1.7 mm in-plane spatial resolution. A total of $n = 8$ healthy volunteers were imaged. Two 0.1 mmol/kg doses of Gadavist were administered 20 to 30 minutes apart, such that the second scan started with a stable but nonzero initial concentration of Gd. CMR multitasking was implemented using a saturation recovery (SR)–prepared FLASH sequence, imaging three time dimensions (Fig. 7a–b): 42 saturation times (up to 300 ms) at 15 cardiac phases and 47.2 ± 4.8 cardiac cycles (as many cycles as occurred during the total elapsed time of the scan, depending on the subject's heart rate). This resulted in a total of 29,767 ± 3,026 images from 45 s of data acquisition. Compared to Cartesian Nyquist sampling of 29,767 ± 3,026 images, this corresponds to R=378 ± 38; if the saturation times were instead binned to only eight saturation times, this would correspond to R=72 ± 7. MBF was assessed at end-diastole via Fermi deconvolution[38] of R_1-derived contrast agent concentration time curves (Fig. 7c–d).

A two-way ANOVA (Table 1) indicated a nonsignificant difference (p=0.44) between repetitions and a nonsignificant difference (p=0.47) between six mid-ventricular segments. MBF values from both boluses (First bolus: 1.18 ± 0.35 g/mL/min; Second bolus: 1.23 ± 0.32 g/mL/min) were within the normal range reported in previous literature[40]. The within-segment standard deviation was 0.30 g/mL/min.

DISCUSSION

The results show that free-breathing, ECG-free T_1 mapping with CMR multitasking produces myocardial T_1 values similar to MOLLI, a leading breath-hold, ECG-triggered technique and to ground truth T_1 values in vials placed along a subject's chest. The *in vivo* measurements are repeatable, with a 4.8% CoV. CMR multitasking also enables quantification of T_1 throughout the cardiac cycle and at multiple respiratory phases. Additionally performing multitasking T_1 mapping post-contrast (i.e., 10–20 minutes after the administration of Gd) has the potential to also allow quantification of extracellular volume fraction (ECV) for comprehensive evaluation of myocardial fibrosis. Extension of the method to an additional spatial dimension (i.e., a slice dimension) — which was not explored in this current work — would enable whole-heart T_1 quantification without ECG-gating, breath-holds, or respiratory navigators.

Free-breathing ECG-free T_1-T_2 mapping with CMR multitasking produces values with slight biases compared to MOLLI (a −28 ms bias in T_1 in healthy volunteers and a −37 ms bias in MI patients) and T_2-SSFP mapping (a −2.2 ms bias in T_2 and a +2.5 ms bias in MI patients). The <6% difference between CMR multitasking mean values and reference mean values is well within the range of differences previously observed between parameter mapping methods. For example, a study of myocardial T1 mapping methods at 1.5 T found that ShMOLLI produced T_1 values with a −102 ms (−9.6%) bias in comparison to MOLLI

Author Manuscript Author Manuscript Author Manuscript Author Manuscript

and a −260 ms (−21.5%) bias in comparison to SAPPHIRE[31]. Preparation scheme differences (i.e., IR or T_2prep magnetization preparation vs. T2IR preparation) and sequence differences (i.e., SSFP vs. FLASH) may contribute to the bias between methods. For example, in 2D imaging, blood flowing into the myocardium is not initially in steady-state, which affects the apparent myocardial T_1 value[41]; because different preparation schemes and pulse sequences induce different spin behaviours during the approach to steady-state, they may have different effects on apparent myocardial T_1. Note that the general CMR multitasking framework is compatible with multiple preparation schemes and pulse sequences, including combinations not explored in this work. Extension of the T_1-T_2 mapping method to an additional spatial dimension with volumetric excitation would not be subject to the same inflow properties of 2D imaging, and may reduce this bias further. Furthermore, 3D T_1-T_2 mapping would allow comprehensive whole-heart myocardial tissue characterization applicable to fibrosis, oedema, and any other condition indicated by T_1 or T_2.

In acute MI patients, multitasking T_1 and T_2 measurements were even more highly correlated to reference methods than in the healthy cohort, likely due to the increased range of T_1 and T_2 values in the patient population. Native T_1 and T_2 mapping were each predictive of LGE status, for the reference methods as well as for multitasking. The combination of both native T_1 and T_2 from multitasking was capable of more accurately classifying LGE status in the pilot data (91% sensitivity and 91% specificity) than were single measurements from either method alone — indicating the potential value of joint T_1-T_2 mapping using multitasking.

CMR multitasking for non-ECG first-pass myocardial perfusion T_1 mapping has a demonstrated capability to perform single-bolus quantitative myocardial perfusion. The study shows that MBF measurements are reproducible despite differences in initial contrast agent concentration between boluses spaced only 20–30 minutes apart (the within-segment standard deviation of 0.30 g/mL/min compares favourably with non–T_1-mapping ECG-free perfusion methods[42]). Potential future directions include evaluation of the method for stress perfusion, extension to a third spatial dimension for whole-heart evaluation, and incorporation of motion correction for free-breathing acquisition. Validation of MBF against nuclear medicine would also be an important step in translating first-pass myocardial perfusion T_1 mapping to the clinic.

As these results demonstrate, MR multitasking addresses many long-standing limitations in quantitative CMR: 1) it efficiently handles motion, removing dependence on ECG control and/or on breath holds and providing a potential means of performing quantitative CMR in arrhythmia patients; 2) it corrects the inaccuracy involved in quantifying contrast agent concentration from T_1-weighted images, allowing quantification from a single bolus of contrast; and 3) it simplifies workflow, using a single setup-free scan to produce co-registered, motion-resolved parameter maps instead of a sequence of misaligned scans, each involving a complex setup process to determine the ECG trigger delay time, respiratory gating window centre and width, and/or timing parameters for selecting proper image contrast.

Author Manuscript Author Manuscript Author Manuscript Author Manuscript

These solutions were enabled by the development of a new LRT imaging method designed particularly for our CMR multitasking framework, allowing flexible sampling and efficient, factored tensor reconstruction. It differs from MR fingerprinting in its ability to image motion and DCE in addition to NMR relaxation. Moreover, because CMR multitasking with LRT imaging can sweep a wide range of "natural" imaging contrasts (i.e., as opposed to MR fingerprinting's randomized image contrasts), the images produced by multitasking may also be themselves directly useful for diagnosis. LRT imaging also differs from other multidimensional imaging approaches such as XD-GRASP by specifically addressing the curse of dimensionality, scaling linearly in both scan time and computational complexity to higher dimensionality. Furthermore, where XD-GRASP exploits "local" similarity of images by implicitly assuming piecewise constant evolution laterally along each time dimension, LRT imaging globally exploits image correlation both laterally and diagonally throughout the entire multidimensional temporal space.

This work provides a proof-of-concept of CMR multitasking for various ECG-free imaging measurements, but it also has the potential to enable or improve other measurements as well, including contrast-scout–free dark-blood late gadolinium enhancement (a possible application of the current T2IR-FLASH multitasking method), cardiac-resolved spectroscopic imaging (replacing the NMR relaxation dimensions with a spectral dimension[22]), myocardial tagging with T_1 fade correction (incorporating tag timing relative to the cardiac cycle as a time dimension), multicontrast and quantitative angiography (another possible application of the current IR-FLASH or T2IR-FLASH multitasking methods), motion-resolved fingerprinting (incorporating a "fingerprint" dimension for signal evolution from a pseudorandom pulse sequence), and more. Furthermore, the motion capabilities of multitasking have yet to be fully exploited: for example, quantitative imaging in arrhythmia patients would demonstrate the benefit of ECG-free multitasking to make quantitative CMR available to a wider range of subjects. Our preliminary results warrant more in-depth evaluation of the potential benefits of motion-resolved quantitative imaging beyond ECG independence, e.g., the analysis of changes in quantitative metrics throughout the cardiac cycle to reveal physiological information that goes undetected by other approaches. Fully exploiting the workflow benefits of MR multitasking would allow a radical departure from the standard CMR exam, potentially enabling a "push-button" CMR exam that comprehensively quantifies cardiovascular health — obtaining, for example, whole-heart T_1 maps pre- and post-contrast (for calculating native T_1 and ECV), T_1-mapped first-pass perfusion, and LGE images in a single 15 min, continuous, setup-free scan.

METHODS

Image model

CMR multitasking represents a cardiovascular image as a multidimensional function $I(\mathbf{x}, t_1, t_2, \cdots, t_N)$ of spatial location $\mathbf{x}$ and of N time dimensions $t_1, t_2, \cdots, t_N$. Each time dimension corresponds to a different "task" to be resolved; example time dimensions correspond to cardiac motion, respiratory motion, time since magnetization preparation (the signal evolution along which is dependent on tissue property parameters such as T_1 and T_2), and time elapsed since the start of imaging (useful for depicting the passage of contrast agent

Author Manuscript Author Manuscript Author Manuscript Author Manuscript

through tissue). The image I can be represented in discretized form as an $(N+1)$-way tensor (or multidimensional array) $\mathscr{A}$ with elements $A_{jkm\cdots q} = I(\mathbf{x}_j, t_{1,k}, t_{2,m}, \cdots, t_{N,q})$, where the first tensor dimension indexes the set of J voxel locations $\left\{\mathbf{x}_j\right\}_{j=1}^{J}$ and each other tensor dimension indexes one of the time dimensions (e.g., if t_1 corresponds to cardiac motion, then $\left\{t_{1,k}\right\}_{k=1}^{K}$ indexes K cardiac phases). Recovery of the entire tensor $\mathscr{A}$ at the Nyquist sampling rate would be subject to the curse of dimensionality, wherein the number of samples required increases exponentially with the number of dimensions being imaged, leading to impractical scan times. However, scan time can be heavily reduced by exploiting spatiotemporal correlation[10], specifically by modelling the tensor $\mathscr{A}$ as low-rank, such that the degrees of freedom in $\mathscr{A}$ increase linearly rather than exponentially[7]. We employ the Tucker form[43] of the low-rank tensor decomposition, which reduces $\mathscr{A}$ to the product of a core tensor and $N+1$ factor matrices,

$$\mathscr{A} = \mathscr{G} \times_1 \mathbf{U}_{\mathbf{x}} \times_2 \mathbf{U}_{t_1} \times_3 \mathbf{U}_{t_2} \times_4 \cdots \times_{(N+1)} \mathbf{U}_{t_N}, \quad (1)$$

where the $\times_i$ operator denotes the ith mode product[7], the factor matrix $\mathbf{U}_{\mathbf{x}} \in \mathbb{C}^{J \times L_0}$ contains L_0 spatial basis functions (or basis images) with J voxels each, each factor matrix $\mathbf{U}_{t_i}$ contains L_i basis functions for the ith time dimension t_i (e.g., $\mathbf{U}_{t_1} \in \mathbb{C}^{K \times L_1}$ contains L_1 temporal basis functions of length K), and where $\mathscr{G} \in \mathbb{C}^{L_0 \times L_1 \times \cdots \times L_N}$ is the core tensor governing the interaction between factor matrices (Supplementary Fig. 1). The factor matrices and core tensor have far fewer elements than the $JKM\cdots Q$ elements in $\mathscr{A}$; this reduction in the degrees of freedom lowers sampling requirements, allowing highly accelerated scanning.

This reduction in degrees of freedom highlights one of the primary benefits of low-rank tensor imaging over low-rank matrix imaging, wherein the image is modelled as a low-rank matrix $\mathbf{A}_{(1)}$ (the subscript (n) denotes mode-n unfolding or flattening of the tensor into a matrix[7]). Modelling $\mathbf{A}_{(1)}$ as a rank-L_0 matrix $\mathbf{A}_{(1)} = \mathbf{U}_{\mathbf{x}}\mathbf{\Phi}$, where $\mathbf{\Phi} \in \mathbb{C}^{L_0 \times KM\cdots Q}$, does reduce the degrees of freedom from $JKM\cdots Q$ to $L_0[J + (KM\cdots Q) - L_0]$, but this still grows exponentially with the number of time dimensions. In contrast, the degrees of freedom in a Tucker rank-$(L_0, L_1, \cdots, L_N)$ tensor are upper bounded by the number of elements in the factor matrices and core tensor: $(L_0J + L_1K + L_2M + \cdots, + L_NQ + (L_0\ L_1 \cdots L_N)$; for imaging scenarios, this bound is dominated by the first term, L_0J. Consider an example of cardiac- and respiratory-resolved T_1-T_2 mapping with 160^2 voxels, 16 cardiac phases, 5 respiratory bins, 344 inversion times, and 5 T_2prep durations: the $160^2 \times 16 \times 5 \times 344 \times 5$ tensor $\mathscr{A}$ has 3.52 billion elements, a rank-42 matrix $\mathbf{A}_{(1)}$ has 6.85 million degrees of freedom, and a Tucker rank-(42,8,4,5,4) tensor $\mathscr{A}$ has a maximum of 1.10 million degrees of freedom (a bound dominated by the L_0J term, which is equal to 1.08 million). In this example, the low-rank tensor model yields a minimum 3,190-fold reduction in degrees of freedom.

Author Manuscript Author Manuscript Author Manuscript Author Manuscript

Low-rank tensor imaging with multiple time dimensions has further practical benefits over low-rank matrix imaging of a single generalized time dimension. First, where low-rank matrix imaging requires acquisition of at least L_0 samples at each of the $KM\cdots Q$ time points $\left\{\left(t_{1,k}, t_{2,m}, \cdots, t_{N,q}\right)\right\}_{k=1,m=1,\ldots,q=1}^{K,M,\ldots,Q}$ in order to define each individual column of $\mathbf{\Phi}$, low-rank tensor imaging can instead recover images at time points from which no samples were obtained (e.g., for motion state/contrast combinations not experienced during the scan). This is because in LRT imaging, the higher-dimensional generalization of $\mathbf{\Phi}$ — the tensor $\mathit{\Phi} \in \mathbb{C}^{L_0 \times K \times M \times \cdots \times Q}$ such that $\mathscr{A} = \mathit{\Phi} \times_1 \mathbf{U_x}$ — is itself low-rank, and can therefore be constructed from the individual temporal bases and the core tensor according to $\mathit{\Phi} = \mathscr{G} \times_2 \mathbf{U}_{t_1} \times_3 \mathbf{U}_{t_2} \times_4 \cdots \times_{(N+2)} \mathbf{U}_{t_N}$. This constraint on the structure of $\mathit{\Phi}$ allows data from missing time points to be filled in from multiple directions (i.e., along multiple time dimensions) using the appropriate basis functions. Second, the use of individual bases for each time dimension optionally allows the pre-determination of factor matrices relating to non-physiological time dimensions (e.g., NMR relaxation), uncorrupted by measurement noise (Supplementary Fig. 2). Strategies to exploit both these advantages are discussed in the subsection on tensor subspace estimation.

Sampling and reconstruction strategies

For the purposes of notation, it is useful to express equation (1) in matrix form as

$$\mathbf{A}_{(1)} = \mathbf{U_x}\mathbf{G}_{(1)}(\mathbf{U}_{t_N} \otimes \mathbf{U}_{t_{N-1}} \otimes \cdots \otimes \mathbf{U}_{t_1})^T, \quad (2)$$

where the $\otimes$ operator denotes the Kronecker product. With this form, the multichannel MR signal $\mathbf{d}$ from tensor $\mathscr{A}$ is expressed as $\mathbf{d} = \Omega(\mathbf{FSA}_{(1)})$, where $\mathbf{S}$ applies coil sensitivity maps to $\mathbf{A}_{(1)}$, where $\mathbf{F}$ applies the appropriate spatial encoding operator (most commonly the Fourier encoding operator that transforms $\mathbf{x}$-space to $\mathbf{k}$-space), and where $\Omega(\cdot)$ is the sampling operator corresponding to samples acquired and collected in the vector $\mathbf{d}$. The image tensor $\mathscr{A}$ can then be reconstructed by low-rank tensor completion[44], for example,

$$\widehat{\mathscr{A}} = \arg\min_{\mathscr{A}} \|\mathbf{d} - \Omega(\mathbf{FSA}_{(1)})\|_2^2 + \lambda \sum_{n=1}^{N+1} \|\mathbf{A}_{(n)}\|_* + R(\mathscr{A}), \quad (3)$$

where λ is the rank regularization parameter, $\|\cdot\|_*$ denotes the matrix nuclear norm, and where $R(\cdot)$is an optional additional regularization functional which can be employed to enforce complementary image properties such as transform sparsity.

Practical considerations can prevent image reconstruction per equation (3), especially when $\mathscr{A}$ contains many dimensions. Although the low-rank tensor model frees sampling requirements from the curse of dimensionality, the size of $\mathscr{A}$ is still subject to exponential growth. As a result, the memory requirements of storing $\mathscr{A}$ in uncompressed form alongside the identically-sized auxiliary variables involved in solving equation (3) via singular value

Author Manuscript Author Manuscript Author Manuscript Author Manuscript

decomposition (SVD) thresholding are prohibitive. Furthermore, each iteration of the image reconstruction algorithm could involve operations on every column of $\mathbf{A}_{(1)}$ — which can number in the hundreds of thousands — as well as multiple SVDs of large matrices, all at significant computational expense.

For these reasons, we have chosen to instead reconstruct $\mathscr{A}$ in factored form using an explicit tensor subspace constraint[19]:

$$\widehat{\mathbf{U}}_{\mathbf{x}} = \arg \min_{\mathbf{U}_{\mathbf{x}}} \|\mathbf{d} - \Omega([\mathbf{FSU}_{\mathbf{x}}]\mathbf{\Phi})\|_2^2 + R(\mathbf{U}_{\mathbf{x}}), \quad (4)$$

where $\mathbf{\Phi} = \mathbf{G}_{(1)} (\mathbf{U}_{t_N} \otimes \mathbf{U}_{t_{N-1}} \otimes \cdots \otimes \mathbf{U}_1)^T$. Equation (4) allows compressed storage of $\mathbf{A}_{(1)}$, requires application of $\mathbf{FS}$ only to the L_0 columns of $\mathbf{U}_{\mathbf{x}}$, and avoids SVDs of large matrices. This strategy requires explicit knowledge of $\mathbf{\Phi}$. Noting that $\mathbf{\Phi}$ is constructed from the temporal factor matrices (weighted by the core tensor), and does not contain spatially resolved information, we designate a small subset of **k**-space locations for much more frequent sampling than the rest of **k**-space. This subset of data (the "subspace training data") contains limited spatial information, but contains a wealth of temporal information appropriate for determining $\mathbf{\Phi}$. Collection of the subspace training data $\mathbf{d}_{tr}$ is similar to the collection of self-gating lines[45] and is therefore ideally collected frequently enough to resolve the finest physiological time dimension (in this case, cardiac motion). This allows $\mathbf{d}_{tr}$ to additionally be used for cardiac and respiratory phase identification, as described in the Supplementary Method.

The remaining subset of the data (the "imaging data") determines the spatial characteristics of $\mathbf{U}_{\mathbf{x}}$, and should therefore cover **k**-space as appropriate for the desired spatial resolution and field of view. This sampling scheme is preferably designed so that there is incoherence between the sampling operator and the factor matrices[46]. This implies that ordered uniform sampling could present a problem if it were coherent with the temporal basis functions, e.g., periodic sampling synchronized to the respiratory cycle, the cardiac cycle, or the magnetization preparation period. In this sense, the performance of ordered uniform sampling would actually be aided by heart rate and respiratory rate variability. The magnetization preparation schedule is typically exactly periodic, but the preparation period and sampling period can be chosen to avoid synchronization with each other. To avoid these issues, sampling schemes such as golden-angle radial sampling or randomized Cartesian sampling can be employed to provide incoherence even in the case of periodic motion.

Tensor subspace estimation

Once the motion states have been identified, the subspace training data can be reshaped into a ($\mathbf{k}$, t_1, t_2, ⋯, t_N)-space tensor $\mathscr{D}_{tr}$. This subspace training data will cover the contrast weighting/motion state combinations experienced during the scan, but typically will not cover every possible contrast weighting/motion state combination. As a result, this tensor will be incomplete. Note however, that because $\mathscr{D}_{tr}$ is constructed from only the most frequently sampled **k**-space trajectories, it is much smaller and far more densely sampled

Author Manuscript Author Manuscript Author Manuscript Author Manuscript

than the imaging data as a whole; this allows recovery via small-scale low-rank tensor completion, e.g. by:

$$\widehat{\mathscr{D}}_{\mathrm{tr}} = \arg \min_{\mathscr{D}_{\mathrm{tr}}} \|\mathbf{d}_{\mathrm{tr}} - \Omega_{\mathrm{tr}}(\mathscr{D}_{\mathrm{tr}})\|_2^2 + \lambda \sum_{n=1}^{N+1} \|\mathbf{D}_{\mathrm{tr},(n)}\|_* + R(\mathscr{D}_{\mathrm{tr}}), \quad (5)$$

where $\mathbf{d}_{\mathrm{tr}}$ is the subset of measured data used for subspace training and where $\Omega_{\mathrm{tr}}(\cdot)$ retains only the training samples. Because equation (5) requires no Fourier transforms and because it involves only a small subset of **k**-space locations, it is far less computationally expensive than the full-scale tensor completion problem in equation (3). Once the subspace training data tensor is completed, the required matrix $\mathbf{\Phi}$ can be quickly extracted from $\hat{\mathscr{D}}_{\mathrm{tr}}$, for example by truncating the SVD of $\hat{\mathbf{D}}_{\mathrm{tr},(1)}$ or the higher-order SVD (HOSVD)[47] of $\hat{\mathscr{D}}_{\mathrm{tr}}$.

Depending on the application, the temporal basis functions for some time dimensions can optionally be pre-determined even before any data is collected. Consider the example where T_1 relaxation corresponds to the Nth time dimension, t_N Because T_1 relaxation is physically governed by the well-known Bloch equations, a training dictionary of physically feasible signal curves can be readily generated ahead of time. The SVD of this training dictionary yields the factor matrix $\mathbf{U}_{t_N}$, the component of $\mathbf{\Phi}$ that contains relaxation basis functions. Note that the subspace spanned by $\mathbf{U}_{t_N}$ is not limited to signal curves in the training dictionary, but rather to curves correlated with the training curves. In this scenario, equation (5) can be adapted to be partially constrained by the Bloch equations via the available $\mathbf{U}_{t_N}$:

$$\widehat{\mathscr{D}}_{\mathrm{tr}} = \arg \min_{\mathscr{D}_{\mathrm{tr}} \in \mathscr{Y}} \|\mathbf{d}_{\mathrm{tr}} - \Omega_{\mathrm{tr}}(\mathscr{D}_{\mathrm{tr}})\|_2^2 + \lambda \sum_{n=1}^{N} \|\mathbf{D}_{\mathrm{tr},(n)}\|_* + R(\mathscr{D}_{\mathrm{tr}}), \quad (6)$$

where $\mathscr{Y}$ is a tensor subspace defined from the columns of $\mathbf{U}_{t_N}$. Supplementary Fig. 2 compares T_1 relaxation basis functions pre-determined from a training dictionary to T_1 relaxation basis functions learned from measured subspace training data using equation (5). The Supplementary Note describes the effects of dictionary-based subspace training on T_1 fitting.

Native T_1 mapping: Methodology

For native myocardial T_1 mapping, the multitasking sequence generated T_1 contrast by applying an IR magnetization preparation pulse every 2.5 s followed by 5° FLASH readouts (T_R = 3.6 ms, T_E = 1.6 ms) throughout the entire recovery period (Supplementary Fig. 3); odd-numbered readouts followed a golden-angle radial sampling schedule (comprising the imaging data), and even-numbered readouts acquired the 0° radial spoke (comprising the subspace training data). An analysis of the Cramér-Rao bound on the variance of the estimator for T_1 indicated that low–flip-angle/short-T_R combinations were effective for mapping native myocardial T_1; the 2.5 s recovery period was chosen so that tissues with T_1 less than or equal to that of blood would approximately reach steady-state by the time of the next inversion pulse. A total of 24 IR pulses were applied for a total scan time of 60 s. The

Author Manuscript Author Manuscript Author Manuscript Author Manuscript

scan was free-running (i.e., continual-acquisition) with no ECG synchronization. Three time dimensions were used, representing cardiac motion (16 cardiac phases), respiratory motion (5 respiratory phases), and T_1 recovery (344 inversion times). The 344 inversion times represent half of the 688 total inversion times, corresponding to the golden-angle radial readout times. The use of this high number of inversion times (as opposed to a more typical number such as eight[28]) avoids the temporal blurring which would result from grouping neighbouring radial acquisitions with different T_1-weightings. The number of cardiac phases was chosen to give an approximately 50 ms cardiac bin width (for the case of a 75-bpm heart rate), which in most cases should be short enough to map T_1 at end-systole with minimal temporal blurring; the number of respiratory bins was chosen empirically. A training dictionary of 31,815 IR-FLASH signal curves was generated from the Bloch equations according to

$$A\frac{1-e^{-T_R/T_1}}{1-e^{-T_R/T_1}\cos\alpha}\left[1+(B-1)\left(e^{-T_R/T_1}\cos\alpha\right)^n\right]\sin\alpha, \quad (7)$$

where the amplitude A absorbs proton density, T_2^* weighting, and receive coil sensitivity, where n is the readout index, α is the FLASH flip angle, and $B = \cos\alpha_{prep}$, where is α_{prep} is the preparation pulse flip angle (ideally 180° for inversion recovery). The training dictionary was generated for 101 T_1 values logarithmically spaced from 100 ms and 3 s, 15 α values in half-degree increments from 0.5° to 7.5° (addressing B_1 transmit inhomogeneity for the FLASH pulses), and 21 B values linearly spaced from −1 to −0.5 (addressing B_1 transmit inhomogeneity for the preparation pulse as well as a potentially incomplete approach to steady-state); five T_1 relaxation basis functions were defined from the SVD of this training dictionary. The training data $\hat{\mathcal{D}}_{tr}$ were then completed per equation (6) using a temporal total variation regularization (TV) functional along the cardiac and respiratory dimensions[9] for $R(\cdot)$, $\mathbf{\Phi}$ was defined from the SVD of $\hat{\mathbf{D}}_{tr,(1)}$ using $L_0 = 32$, and $\hat{\mathbf{U}}_{\mathbf{x}}$ was calculated per equation (4) using a spatial TV regularization functional for $R(\cdot)$. After image reconstruction, voxel-wise T_1, A, α, and B were fit from equation (7).

Native T_1 mapping: Comparison to reference methods

To evaluate the accuracy and repeatability of native myocardial T_1 mapping using CMR multitasking, $n = 10$ healthy human volunteers were recruited. Three scans each were collected of: diastolic T_1 maps from ECG-triggered, breath-held SSFP MOLLI 5(3)3; and cardiac- and respiratory-resolved T_1 maps from the proposed non-ECG, free-breathing multitasking method. One mid-ventricular short-axis slice with 1.7 mm in-plane spatial resolution and 8 mm slice thickness was imaged using each method; T_1 values in six myocardial segments were compared at end-diastole and end-expiration. Repeatability of each method was assessed by the coefficient of variation (CoV), calculated as the root-mean-square (RMS) within-segment standard deviation (WSSD) divided by the population mean.

To further evaluate the accuracy of multitasking T_1 mapping, a combined *in vivo* and *in vitro* experiment was performed by placing ten phantom vials along the chest of a healthy

Author Manuscript Author Manuscript Author Manuscript Author Manuscript

volunteer. Cardiac- and respiratory-resolved T_1 maps were collected using multitasking; the mean T_1 of each vial was compared to the ground truth T_1 values (which ranged from 480 ms to 1987 ms, as established from a separate *in vitro*–only IR spin echo experiment).

Native T_1-T_2 mapping: Methodology

For native myocardial T_1-T_2 mapping, T_1-T_2 contrasts were generated by cycling through a series of five hybrid T2IR preparation pulses with durations $T_{E,prep}$ = 12, 20, 30, 40, 50 ms, each followed by 5° FLASH readouts (T_R = 3.6 ms, T_E = 1.6 ms) throughout the entire 2.5 s recovery period (Supplementary Fig. 4). The T2IR pulse consists of an adiabatic T_2-preparation[48] with BIR-4 refocusing[49], modified to apply a 90° tip-down pulse instead of a 90° tip-up pulse after refocusing (thereby achieving the effect of a 90° tip-up followed by 180° inversion[50]). The T_2prep durations were chosen to be approximately uniformly spaced between the shortest T_2prep time allowed by the system (12 ms) and a T_2prep time on the order of native myocardial T_2 at 3 T (50 ms). Sampling was performed according to the previously-described golden-angle sampling scheme modified to collect subspace training data every other readout. A total of 35 T2IR pulses were applied for a total scan time of 88 s. Four time dimensions represented cardiac motion (16 cardiac phases), respiratory motion (5 respiratory phases), T_1 recovery (344 inversion times), and T_2prep duration (5 durations). As in native T_1 mapping, five T_1 relaxation basis functions were defined from the SVD of a Bloch signal training dictionary, but with an expanded range of inversion pulse flip angles (i.e., the 21 B values were linearly spaced from −1 to 0) in order to address multiple signal starting points due to T_2 decay during T2IR preparation. T_2 relaxation basis functions were not pre-determined due to the complexity of simulating B_0 inhomogeneity. Reconstruction was performed per equations (6) and (4) using L_0 = 42 and the same regularization schemes as for native T_1 mapping. Voxel-wise T_1, T_2, A, α, and B were fit from

$$A\frac{1-e^{-T_R/T_1}}{1-e^{-T_R/T_1}\cos\alpha}\left[1+(Be^{-T_{E,\,prep}/T_2}-1)\left(e^{-T_R/T_1}\cos\alpha\right)^n\right]\sin\alpha\,. \quad (8)$$

Native T_1-T_2 mapping: Comparison to reference methods

To evaluate the accuracy and repeatability of native myocardial T_1-T_2 mapping using CMR multitasking, n = 10 healthy human volunteers were recruited for imaging. Three scans each were collected of: diastolic T_1 maps from ECG-triggered, breath-held SSFP MOLLI 5(3)3; diastolic T_2 maps from ECG-triggered, breath-held T_2prep-SSFP mapping; and cardiac- and respiratory-resolved T_1-T_2 maps from the proposed non-ECG, free-breathing multitasking method. One mid-ventricular short-axis slice with 1.7 mm in-plane spatial resolution and 8 mm slice thickness was imaged using each method; T_1 and T_2 values in six myocardial segments were compared at end-diastole and end-expiration, and the repeatability of each method was assessed by the RMS WSSD and CoV.

To investigate the potential of multitasking to assess cardiac function, end-systolic and end-diastolic left ventricular areas were compared between non-ECG, free-breathing T2IR-FLASH multitasking images and conventional cine imaging. Retrospectively ECG-gated

Author Manuscript Author Manuscript Author Manuscript Author Manuscript

bSSFP cine images were collected during an end-expiration breath hold at 1.3 mm in-plane spatial resolution and 8 mm slice thickness, with 25 frames per cardiac cycle. End-expiration dark-blood images were extracted from the T2IR-FLASH multitasking reconstructions. Trabeculae and papillary muscles were considered part of the LV blood pool when drawing endocardial contours.

To evaluate the diagnostic utility of native T_1-T_2 mapping using CMR multitasking, $n = 10$ patients with acute myocardial infarction (MI) were recruited for imaging. One scan each was collected of: diastolic T_1 maps from MOLLI 5(3)3, diastolic T_2 maps from T_2prep-SSFP mapping, and cardiac- and respiratory-resolved T_1-T_2 maps from T2IR-FLASH multitasking. Mid-ventricular or basal short-axis slices with 1.7 mm in-plane spatial resolution and 8 mm slice thickness were imaged; T_1 and T_2 values in six myocardial segments per subject were compared at end-diastole and end-inspiration. In two subjects, only five myocardial segments were available for analysis, as the basal slice selected for mapping intersected the LV outflow tract. After native parameter mapping, late gadolinium enhancement (LGE) imaging was performed to assess the extent of MI.

Myocardial perfusion T_1 mapping

For first-pass myocardial perfusion T_1 mapping, T_1 contrasts were generated using SR magnetization preparation followed by 10° FLASH readouts (T_R = 3.6 ms, T_E = 1.6 ms) throughout a 300 ms recovery period (Supplementary Fig. 5). The short recovery period and SR preparation scheme were chosen to reduce blood inflow effects, as accurate blood signal quantification is vital to accurate quantification of MBF. Golden-angle sampling with subspace training data collected every other readout was performed. A total of 150 SR periods were acquired for a total scan time of 45 s. Four time dimensions represented cardiac motion (15 cardiac phases), respiratory motion (5 respiratory phases), T_1 recovery (42 saturation times), and elapsed time depicting DCE (one bin per cardiac cycle). Five T_1 relaxation basis functions were defined according to the same process as for native T_1 mapping, but with 30 α values in half-degree increments from 0.5° to 15° and 21 B values linearly spaced from −0.25 to 0.25. Reconstruction was performed per equation (6) using temporal TV regularization along the cardiac, respiratory, and elapsed time (DCE) dimensions and equation (4) using $L_0 = 36$ and spatial TV regularization.

The intrasession reproducibility of MBF quantification using myocardial perfusion T_1 mapping was assessed in $n = 8$ healthy human volunteers by administering two 0.1 mmol/kg doses of Gadavist (4 mL/s injection rate, followed by 20 mL saline flush) 20 to 30 minutes apart (i.e., long enough for the first bolus to reach a steady-state). Subjects were instructed to hold their breath for as much of the scan as possible, followed by shallow breathing. One mid-ventricular short-axis slice with 1.7 mm in-plane spatial resolution and 8 mm slice thickness was imaged each time. To quantify MBF, $T_1(t)$, A, α, and B were fit according to

$$A\frac{1-e^{-T_R/T_1(t)}}{1-e^{-T_R/T_1(t)}\cos\alpha}\left[1+(B-1)\left(e^{-T_R/T_1(t)}\cos\alpha\right)^n\right]\sin\alpha, \quad (9)$$

Author Manuscript Author Manuscript Author Manuscript Author Manuscript

from the LV blood pool and six myocardial segments at end-diastole. Contrast agent concentration $Gd(t)$ was calculated as

$$Gd(t) = \Delta R_1(t)/\gamma = \left(\frac{1}{T_1(t)} - \frac{1}{T_{1,\,\mathrm{pre}}}\right)/\gamma, \quad (10)$$

where γ is the T_1 relaxivity of the contrast agent (5 $mM^{-1}{\cdot}s^{-1}$)[51, 52] and $T_{1,\mathrm{pre}}$ is the baseline T_1 (i.e., the mean pre-contrast T_1). Fermi deconvolution[38] of each myocardial $Gd(t)$ by the left ventricular blood pool $Gd(t)$ yielded the MBF for each myocardial segment. A two-way ANOVA was performed to assess differences in MBF between segments and repetitions; repeatability of each method was quantified by the RMS WSSD and CoV.

Materials

All data were acquired on a 3 T Siemens Verio scanner. Multitasking reconstructions, multitasking parameter fitting, and statistical analyses were performed in MATLAB R2015b on a workstation equipped with two 2.70 GHz 12-core Intel Xeon CPUs, an NVIDIA Quadro K6000 GPU, and 256 GB of RAM. Median reconstruction time on this workstation was 71 minutes.

Human subjects

All subjects took part under the approval of the Cedars-Sinai Medical Center Institutional Review Board, and informed consent was collected before imaging. The inclusion criteria for the healthy volunteer study were as follows: (i) males and females older than 18 years of age; (ii) no known disease and body-mass index (BMI) under 30; (iii) able to undergo MRI (e.g., no metal implants, no claustrophobia). The inclusion criteria for the patient study were as follows: (i) males and females older than 18 years of age; (ii) acute myocardial infarction; (iii) able to undergo MRI (e.g., no metal implants, no claustrophobia).

Statistical analyses

Differences between reference measurements and multitasking measurements were analysed by two-sided Student's *t*-tests and Pearson's correlation coefficients; differences between myocardial perfusion measurements from different contrast boluses were analysed by a two-way analysis of variance test. Values of $p < 0.05$ were considered statistically significant. Normality was checked by the Shapiro–Wilk test.

Code availability

The multitasking image reconstruction software in the form of MATLAB P-code is available from the authors upon reasonable request.

Data availability

The data supporting the findings of this study are available within the paper and its supplementary information. Segment-wise data underlying Figs. 2–6 and Table 1 are available from the authors upon reasonable request.

Author Manuscript Author Manuscript Author Manuscript Author Manuscript

Supplementary Material

Refer to Web version on PubMed Central for supplementary material.

Acknowledgments

This work was supported by NIH 1R01HL124649 and NIH T32HL116273.

References

1. Moon JC, et al. Myocardial T1 mapping and extracellular volume quantification: a Society for Cardiovascular Magnetic Resonance (SCMR) and CMR Working Group of the European Society of Cardiology consensus statement. J Cardiovasc Magn Reson. 2013; 15:92. [PubMed: 24124732]
2. Giri S, et al. T2 quantification for improved detection of myocardial edema. J Cardiovasc Magn Reson. 2009; 11:56. [PubMed: 20042111]
3. Atkinson D, Burstein D, Edelman R. First-pass cardiac perfusion: evaluation with ultrafast MR imaging. Radiol. 1990; 174:757–762.
4. Christian TF, et al. Absolute myocardial perfusion in canines measured by using dual-bolus first-pass MR imaging. Radiol. 2004; 232:677–684.
5. Lustig M, Donoho D, Pauly JM. Sparse MRI: The application of compressed sensing for rapid MR imaging. Magn Reson Med. 2007; 58:1182–1195. [PubMed: 17969013]
6. Ma D, et al. Magnetic resonance fingerprinting. Nature. 2013; 495:187–192. [PubMed: 23486058]
7. Kolda TG, Bader BW. Tensor decompositions and applications. SIAM Rev. 2009; 51:455–500.
8. Hamilton JI, et al. MR fingerprinting for rapid quantification of myocardial T1, T2, and proton spin density. Magn Reson Med. 2017; 77:1446–1458. [PubMed: 27038043]
9. Feng L, et al. XD-GRASP: Golden-angle radial MRI with reconstruction of extra motion-state dimensions using compressed sensing. Magn Reson Med. 2016; 75:775–788. [PubMed: 25809847]
10. Liang Z-P. Spatiotemporal imaging with partially separable functions. Proc IEEE Int Symp Biomed Imaging; 2007. 988–991.
11. Pedersen H, Kozerke S, Ringgaard S, Nehrke K, Kim WY. k-t PCA: Temporally constrained k-t BLAST reconstruction using principal component analysis. Magn Reson Med. 2009; 62:706–716. [PubMed: 19585603]
12. Huang C, Graff CG, Clarkson EW, Bilgin A, Altbach MI. T2 mapping from highly undersampled data by reconstruction of principal component coefficient maps using compressed sensing. Magn Reson Med. 2012; 67:1355–1366. [PubMed: 22190358]
13. Lam F, Liang ZP. A subspace approach to high-resolution spectroscopic imaging. Magn Reson Med. 2014; 71:1349–1357. [PubMed: 24496655]
14. Fu M, et al. High-resolution dynamic speech imaging with joint low-rank and sparsity constraints. Magn Reson Med. 2015; 73:1820–1832. [PubMed: 24912452]
15. Zhao B, et al. Accelerated MR parameter mapping with low-rank and sparsity constraints. Magn Reson Med. 2015; 74:489–498. [PubMed: 25163720]
16. Tamir JI, et al. T2 shuffling: Sharp, multicontrast, volumetric fast spin-echo imaging. Magn Reson Med. 2017; 77:180–195. [PubMed: 26786745]
17. Trzasko JD, Manduca A. A unified tensor regression framework for calibrationless dynamic, multi-channel MRI reconstruction. Proc Int Soc Magn Reson Med. 2013:603.
18. Yu Y, Jin J, Liu F, Crozier S. Multidimensional compressed sensing MRI using tensor decomposition-based sparsifying transform. PLoS One. 2014; 9:e98441. [PubMed: 24901331]
19. Christodoulou AG, Liang Z-P. 3D dynamic T1 mapping of the myocardium using a time-varying subspace. Proc Int Soc Magn Reson Med. 2015; 2614
20. Christodoulou AG, et al. Fast dynamic electron paramagnetic resonance (EPR) oxygen imaging using low-rank tensors. J Magn Reson. 2016; 270:176–182. [PubMed: 27498337]
21. He J, et al. Accelerated high-dimensional MR imaging with sparse sampling using low-rank tensors. IEEE Trans Med Imaging. 2016; 35:2119–2129. [PubMed: 27093543]

Author Manuscript Author Manuscript Author Manuscript Author Manuscript

22. Ma C, et al. High-resolution dynamic 31P-MRSI using a low-rank tensor model. Magn Reson Med. 2017; 78:419–428. [PubMed: 28556373]
23. Ferreira VM, Piechnik SK, Robson MD, Neubauer S, Karamitsos TD. Myocardial tissue characterization by magnetic resonance imaging: Novel applications of T1 and T2 mapping. J Thorac Imaging. 2014; 29:147. [PubMed: 24576837]
24. Messroghli DR, et al. Modified Look-Locker inversion recovery (MOLLI) for high-resolution T1 mapping of the heart. Magn Reson Med. 2004; 52:141–146. [PubMed: 15236377]
25. Piechnik SK, et al. Shortened Modified Look-Locker Inversion recovery (ShMOLLI) for clinical myocardial T1-mapping at 1.5 and 3 T within a 9 heartbeat breathhold. J Cardiovasc Magn Reson. 2010; 12:69. [PubMed: 21092095]
26. Weingärtner S, et al. Heart-rate independent myocardial T1-mapping using combined saturation and inversion preparation pulses. J Cardiovasc Magn Reson. 2013; 15:P46.
27. Chow K, et al. Saturation recovery single-shot acquisition (SASHA) for myocardial T1 mapping. Magn Reson Med. 2014; 71:2082–2095. [PubMed: 23881866]
28. Xue H, et al. Phase-sensitive inversion recovery for myocardial T1 mapping with motion correction and parametric fitting. Magn Reson Med. 2013; 69:1408–1420. [PubMed: 22736380]
29. von Knobelsdorff-Brenkenhoff F, et al. Myocardial T 1 and T 2 mapping at 3 T: reference values, influencing factors and implications. J Cardiovasc Magn Reson. 2013; 15:53. [PubMed: 23777327]
30. Kellman P, Hansen MS. T1-mapping in the heart: accuracy and precision. J Cardiovasc Magn Reson. 2014; 16:2. [PubMed: 24387626]
31. Roujol S, et al. Accuracy, precision, and reproducibility of four T1 mapping sequences: a head-to-head comparison of MOLLI, ShMOLLI, SASHA, and SAPPHIRE. Radiol. 2014; 272:683–689.
32. Kellman P, Chung YC, Simonetti OP, McVeigh ER, Arai AE. Multicontrast delayed enhancement provides improved contrast between myocardial infarction and blood pool. J Magn Reson Imaging. 2005; 22:605–613. [PubMed: 16215969]
33. Blume U, et al. Interleaved T1 and T2 relaxation time mapping for cardiac applications. J Magn Reson Imaging. 2009; 29:480–487. [PubMed: 19161206]
34. Kvernby S, et al. Simultaneous three-dimensional myocardial T1 and T2 mapping in one breath hold with 3D-QALAS. J Cardiovasc Magn Reson. 2014; 16:102. [PubMed: 25526880]
35. Akçakaya M, et al. Joint myocardial T1 and T2 mapping using a combination of saturation recovery and T2-preparation. Magn Reson Med. 2016; 76:888–896. [PubMed: 26418119]
36. DiBella EV, Chen L, Schabel MC, Adluru G, McGann CJ. Myocardial perfusion acquisition without magnetization preparation or gating. Magn Reson Med. 2012; 67:609–613. [PubMed: 22190332]
37. Sharif B, et al. Non–ECG-gated myocardial perfusion MRI using continuous magnetization-driven radial sampling. Magn Reson Med. 2014; 72:1620–1628. [PubMed: 24443160]
38. Jerosch-Herold M, Wilke N, Stillman AE, Wilson RF. Magnetic resonance quantification of the myocardial perfusion reserve with a Fermi function model for constrained deconvolution. Med Phys. 1998; 25:73–84. [PubMed: 9472829]
39. Chen D, et al. Quantification of myocardial blood flow using non–ECG-triggered MR imaging. Magn Reson Med. 2015; 74:765–771. [PubMed: 25227935]
40. Muehling OM, et al. Regional heterogeneity of myocardial perfusion in healthy human myocardium: assessment with magnetic resonance perfusion imaging. J Cardiovasc Magn Reson. 2004; 6:499–507. [PubMed: 15137334]
41. Lee JH, Li X, Sammi MK, Springer CS. Using flow relaxography to elucidate flow relaxivity. J Magn Reson. 1999; 136:102–113. [PubMed: 9887295]
42. Likhite D, et al. Interstudy repeatability of self-gated quantitative myocardial perfusion MRI. J Magn Reson Imaging. 2016; 43:1369–1378. [PubMed: 26663511]
43. Tucker LR. Some mathematical notes on three-mode factor analysis. Psychometrika. 1966; 31:279–311. [PubMed: 5221127]
44. Liu J, Musialski P, Wonka P, Ye J. Tensor completion for estimating missing values in visual data. IEEE Trans Pattern Anal Mach Intell. 2013; 35:208–220. [PubMed: 22271823]

Author Manuscript Author Manuscript Author Manuscript Author Manuscript

45. Larson AC, et al. Self-gated cardiac cine MRI. Magn Reson Med. 2004; 51:93–102. [PubMed: 14705049]
46. Candès EJ, Tao T. The power of convex relaxation: Near-optimal matrix completion. IEEE Trans Info Theory. 2010; 56:2053–2080.
47. De Lathauwer L, De Moor B, Vandewalle J. A multilinear singular value decomposition. SIAM J Matrix Anal Appl. 2000; 21:1253–1278.
48. Nezafat R, et al. B1-insensitive T2 preparation for improved coronary magnetic resonance angiography at 3 T. Magn Reson Med. 2006; 55:858–864. [PubMed: 16538606]
49. Staewen RS, et al. 3-D FLASH imaging using a single surface coil and a new adiabatic pulse, BIR-4. Invest Radiol. 1990; 25:559–567. [PubMed: 2345088]
50. Brown R, et al. Effect of blood flow on double inversion recovery vessel wall MRI of the peripheral arteries: Quantitation with T2 mapping and comparison with flow-insensitive T2-prepared inversion recovery imaging. Magn Reson Med. 2010; 63:736–744. [PubMed: 20187182]
51. Pintaske J, et al. Relaxivity of gadopentetate dimeglumine (Magnevist), gadobutrol (Gadovist), and gadobenate dimeglumine (MultiHance) in human blood plasma at 0.2, 1.5, and 3 Tesla. Invest Radiol. 2006; 41:213–221. [PubMed: 16481903]
52. Shen Y, et al. T1 relaxivities of gadolinium-based magnetic resonance contrast agents in human whole blood at 1.5, 3, and 7 T. Invest Radiol. 2015; 50:330–338. [PubMed: 25658049]

Author Manuscript Author Manuscript Author Manuscript Author Manuscript

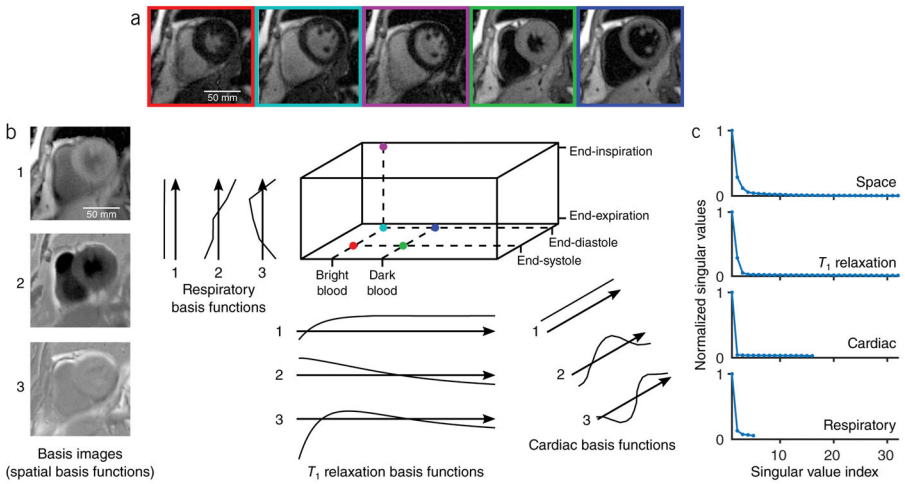

Figure 1.

Illustration and analysis of multiple time dimensions for non-ECG, free-breathing native myocardial T_1 mapping. (**a**) Locations of different images in a space with three time dimensions. Different T_1 weightings lie along the inversion time axis (*horizontal*), different cardiac phases lie along the cardiac time axis (*depth*), and different respiratory phases lie along the respiratory time axis (*vertical*). (**b**) The three most significant basis functions describing each dimension of the image tensor, as reconstructed from 1 min worth of data. (**c**) Singular value curves from the higher-order SVD of 12.3 minutes worth of raw subspace training data (i.e., enough data to cover all motion state/contrast combinations), demonstrating that the singular values decay quickly for all unfoldings of the raw data tensor.

Author Manuscript Author Manuscript Author Manuscript Author Manuscript

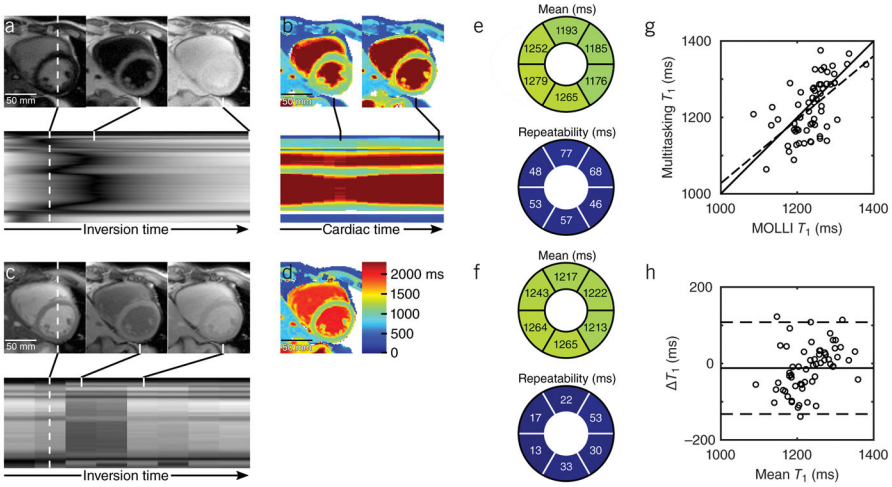

Figure 2.

CMR multitasking for non-ECG, free-breathing native myocardial T_1 mapping. (**a**) CMR multitasking yields finely resolved contrast variation along the inversion time dimension, and produces (**b**) cardiac-resolved T_1 maps. (**c**) MOLLI 5(3)3 relies on ECG-triggering and breath-holding to image eight heart-rate dependent inversion times, and produces (**d**) a static T_1 map. (**e**) Bullseye plots of six mid-ventricular myocardial segments, showing mean diastolic T_1 and measurement repeatability for CMR multitasking in n=10 healthy volunteers; (**f**) corresponding bullseye plots for MOLLI. (**g**) Scatter plot of diastolic T_1 values in n=60 myocardial segments (six segments per subject) from MOLLI and CMR multitasking with line of identity (*solid*) and regression line (*dashed*); (**h**) Bland–Altman plot of the same data.

Author Manuscript Author Manuscript Author Manuscript Author Manuscript

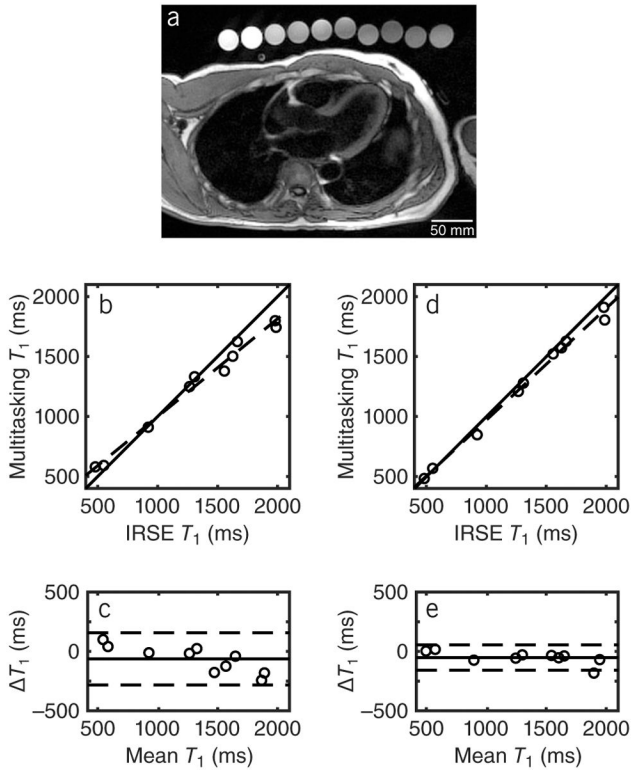

Figure 3.

Comparison of T_1 values in vials placed along a subject's chest. (**a**) Three-chamber view perpendicular to vials. (**b**) Scatter plot of T_1 values in $n = 10$ vials from IR-FLASH CMR multitasking and IRSE with line of identity (*solid*) and regression line (*dashed*); (**c**) Bland–Altman plot of the same data. (**d**) Scatter plot of T_1 values $n = 10$ vials from T2IR-FLASH CMR multitasking and IRSE with line of identity (*solid*) and regression line (*dashed*); (**e**) Bland–Altman plot of the same data.

Author Manuscript Author Manuscript Author Manuscript Author Manuscript

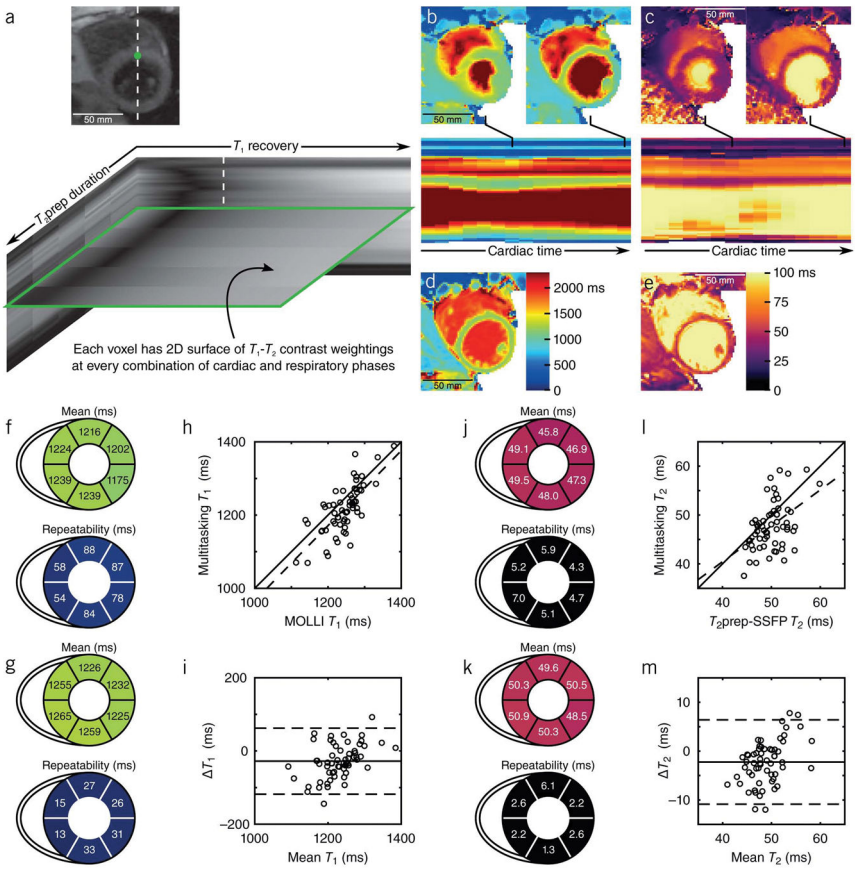

Figure 4.

CMR multitasking for non-ECG, free-breathing joint T_1-T_2 mapping in the myocardium. (**a**) CMR multitasking yields contrast variation along T_1 recovery and T_2prep duration dimensions, producing cardiac-resolved (**b**) T_1 and (**c**) T_2 maps. (**d**) MOLLI 5(3)3 and (**e**) T_2prep-SSFP mapping rely on ECG-triggering and breath-holding to produce separate static parameter maps. (**f**) Bullseye plots of six mid-ventricular myocardial segments, showing mean diastolic T_1 and measurement repeatability for CMR multitasking in n=10 healthy volunteers; (**g**) corresponding bullseye plots for MOLLI. (**h**) Scatter plot of diastolic T_1 values in n=60 myocardial segments (six segments per subject) from MOLLI and CMR multitasking with line of identity (*solid*) and regression line (*dashed*); (**i**) Bland–Altman plot of the same data. (**j**) Bullseye plots showing mean diastolic T_2 and measurement repeatability for CMR multitasking in healthy volunteers; (**k**) corresponding bullseye plots for T_2prep-SSFP. (**l**) Scatter plot of diastolic T_2 values in n=60 myocardial segments (six segments per subject) from T_2prep-SSFP and CMR multitasking with line of identity (*solid*) and regression line (*dashed*); (**m**) Bland–Altman plot of the same data.

Author Manuscript Author Manuscript Author Manuscript Author Manuscript

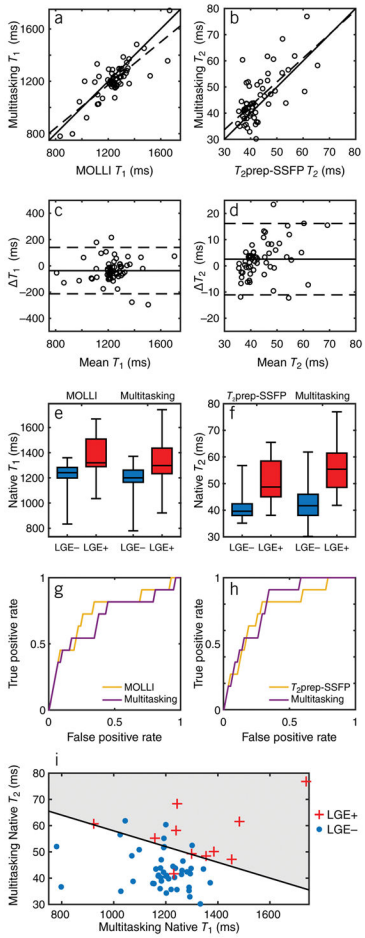

Figure 5.

Native myocardial T_1-T_2 mapping results in 10 patients with acute MI. (**a,b**) Scatter plots of of diastolic (**a**) T_1 and (**b**) T_2 values in n=58 myocardial segments (six segments per subject, excluding two segments which intersected the LV outflow tract) from CMR multitasking and reference methods, with line of identity (*solid*) and regression line (*dashed*); (**c,d**) Bland–Altman plots of the same data. (**e,f**) Box-whisker plots showing median, interquartile range, and full range of values grouped by mapping method and LGE status. (**g,h**) ROC curves for native T_1 and T_2 mapping as predictors of LGE status. (**i**) Multitasking values in a 2D feature space with a decision boundary yielding 91% sensitivity and 91% specificity.

Author Manuscript Author Manuscript Author Manuscript Author Manuscript

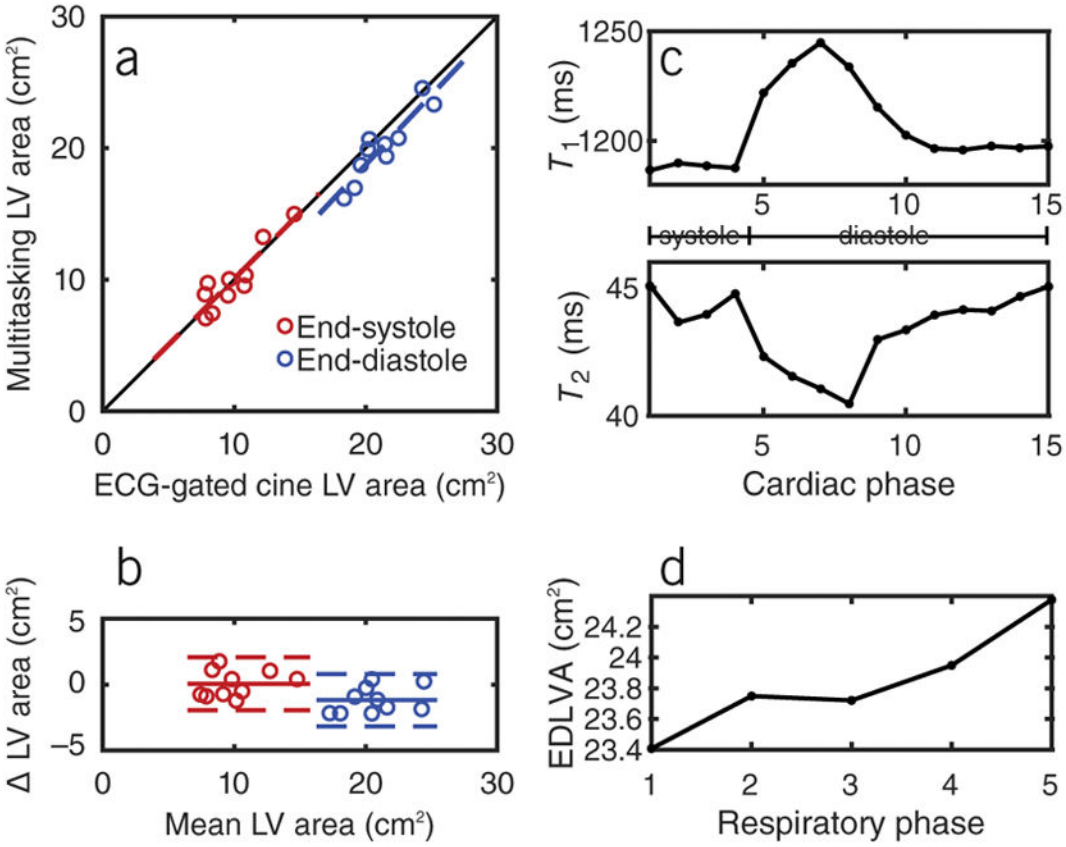

Figure 6.

Example additional measurements available from T2IR-FLASH CMR multitasking (**a**) Scatter plot of in-slice LV areas measured from CMR multitasking and ECG-gated cine imaging in n=10 healthy subjects, with line of identity (*solid*) and regression line (*dashed*); (**b**) Combined Bland–Altman plots of the same data. (**c**) Example T_1 and T_2 variation in the septal myocardium from one subject. (**d**) Example variation of in-slice end-diastolic LV area from end-expiration (resp. phase 1) to end-inspiration (resp. phase 5).

Author Manuscript Author Manuscript Author Manuscript Author Manuscript

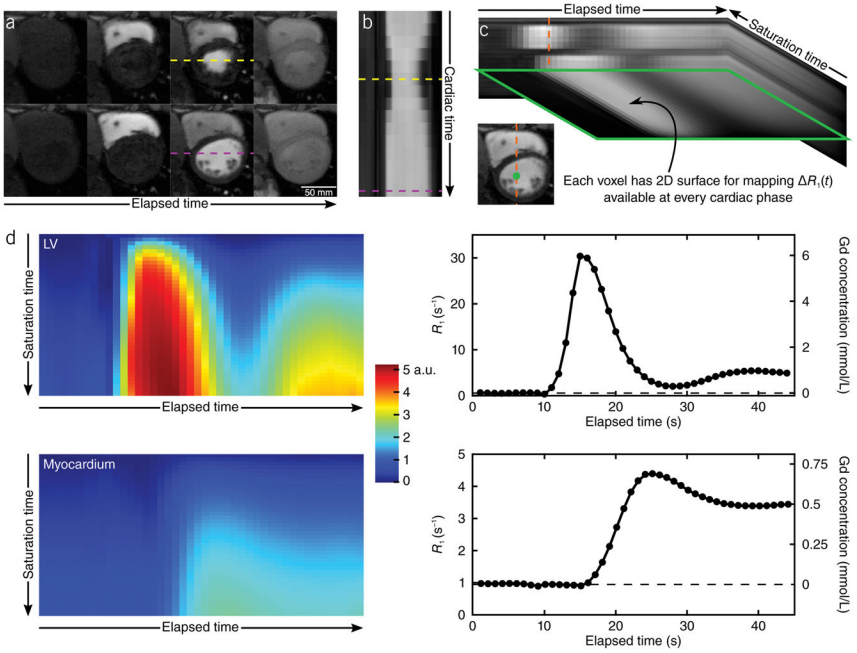

Figure 7.

CMR multitasking for non-ECG, first-pass myocardial perfusion T_1 mapping. (**a**) Contrast agent dynamics are captured for systolic and diastolic cardiac phases, due to (**b**) the method's ability to resolve cardiac motion. (**c**) The combination of the elapsed time dimension (for depicting contrast agent dynamics) and saturation time dimension yield 2D signal intensity surfaces rather than conventional 1D signal intensity curves. (**d**) These signal intensity surfaces are used to map $R_1(t)$, which accounts for signal saturation and directly yields Gd concentration after a linear transformation.

Author Manuscript Author Manuscript Author Manuscript Author Manuscript

Table 1

Two-way ANOVA table indicating nonsignificant differences between repetitions and segments in n=96 myocardial blood flow measurements (six myocardial segments in 8 healthy volunteers, each measured twice).

Source	Sum of Squares	Degrees of Freedom	Mean Squares	*F*	*p*
Segments	0.527	5	0.105	0.92	0.47
Repetition	0.065	1	0.065	0.57	0.44
Error	10.229	89	0.115		
Total	10.821	95			

Nat Biomed Eng. Author manuscript; available in PMC 2018 October 09.